Surface Instability in a Nematic Elastomer

Morgan Barnes,* Fan Feng,* and John S. Biggins†
Department of Engineering, University of Cambridge, Trumpington Street, Cambridge CB2 1PZ, United Kingdom

(Received 13 March 2023; accepted 3 November 2023; published 7 December 2023)

Liquid crystal elastomers (LCEs) are soft phase-changing solids that exhibit large reversible contractions upon heating, Goldstone-like soft modes, and resultant microstructural instabilities. We heat a planar LCE slab to isotropic, clamp the lower surface, then cool back to nematic. Clamping prevents macroscopic elongation, producing compression and microstructure. We see that the free surface destabilizes, adopting topography with amplitude and wavelength similar to thickness. To understand the instability, we numerically compute the microstructural relaxation of a "nonideal" LCE energy. Linear stability reveals a Biot-like scale-free instability, but with oblique wave vector. However, simulation and experiment show that, unlike classic elastic creasing, instability culminates in a crosshatch without cusps or hysteresis, and is constructed entirely from low-stress soft modes.

DOI: 10.1103/PhysRevLett.131.238101

Liquid crystal elastomers (LCEs) are actuating solids that recall the dramatic shape transformations of biological tissues. Microscopically, LCEs are networks of LC polymers [1]. Actuation occurs via the isotropic-nematic phase transition, which biases conformations along the director, generating large elongations on cooling, and muscular contraction on heating [2,3]. Correspondingly, LCEs fabricated with spatial director profiles can actuate into complex surfaces [4] such as cones [5,6] or faces [7,8]. The symmetry breaking character of the isotropic-nematic transition also endows LCEs with Goldstone-like "soft modes" in which deformations induce director rotation at almost zero energy and stress [9,10]. Such modes enable actuation by modest electric fields [11,12] and generate martensitic [13] microstrucural instabilities [14–16]. However, despite progress in idealized cases [16–18], we still lack a realistic coarse-grained constitutive model that accounts for microstructure, preventing analysis of macroscopic LCEs under load.

Mechanical instabilities like buckling provide an attractive additional route to complex morphing without prepatterning. For example, the Biot creasing instability sculpts cusped folds at the free surface of soft solids under compression [19–22], and underpins morphogenesis of villi [23] and sulci or gyri [24]. Here, we combine experiment, theory, and computation to tackle the analogous compressive surface instability in LCEs, which is profoundly enriched by soft modes and microstructure.

Experimentally, we fabricate a monodomain LCE [Supplemental Material (SM) [25], Sec. I] via two-step cross-linking with mechanical programming [2], using commercially available acrylate-functionalized mesogens and thiol-functionalized chain extenders and cross-linkers [8,26]. The resulting film is clear but birefringent at room temperature, reflecting its planar nematic alignment, and

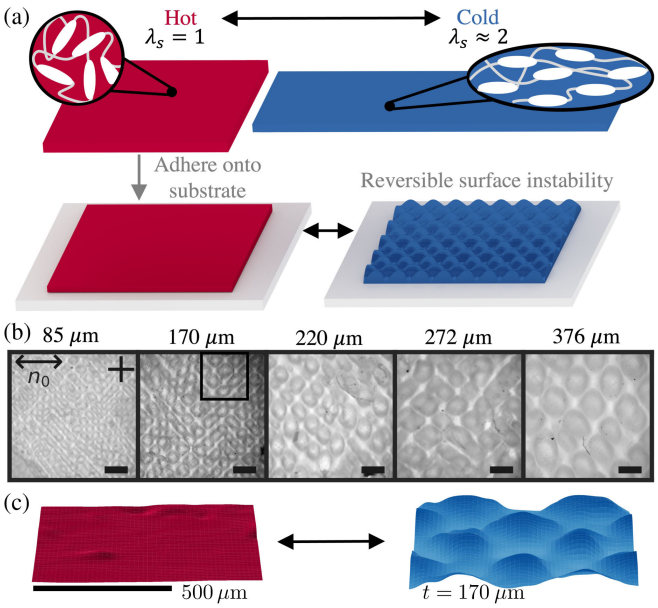

FIG. 1. (a) Schematic of LCE actuation between hot (isotopic) and cold (nematic), and resulting surface instability when adhered to a foundation while hot. (b) Micrographs polarized optical microscopy (POM) of surface instability for varying LCE thicknesses. (Scale bars 500 μm.) (c) Topography changes (boxed region) from optical profliometry (SM, Sec. III [25]), true aspect ratio.

elongates reversibly by a factor of $\lambda_s \approx 2$ on cooling from isotropic to nematic (SM, Fig. S2 [25]). Inspired by observations of creasing in gel slabs that are swollen on a clamped foundation [20,22], we adhere the LCE to a glass slide while isotropic then cool to nematic [Fig. 1(a)]. The slide prevents elongation, placing the LCE in compression, causing turbidity in the LCE indicative of optical-scale microstructure. Moreover, the surface destabilizes, forming a high amplitude crosshatch pattern of topography with wide bumps separated by narrow valleys [Figs. 1(b) and 1(c), and SM [25], Sec. III, Movies M1 and M2]. Topography is reversible on heating (SM [25], Movie M3), and experiments varying LCE thicknesses show amplitude and wavelength are proportional to thickness.

To explain the instability, we first model the LCE as a simple rubber slab undergoing a spontaneous elongation while clamped below, leading to a displacement field $\mathbf{u}$ (from isotropic) and deformation gradient $\mathbf{\Lambda} = \mathbf{I} + \nabla\mathbf{u}$. A standard neo-Hookean rubber with shear modulus μ stores elastic energy density $W_{\rm NH}(\mathbf{\Lambda}) = \frac{1}{2}\mu \mathrm{Tr}(\mathbf{\Lambda}\mathbf{\Lambda}^{\rm T})$, and is strictly incompressible $\mathrm{Det}(\mathbf{\Lambda}) = 1$. Accordingly, the LCE energy is $W_{\rm NH}(\mathbf{\Lambda}\mathbf{\Lambda}_s^{-1})$, where $\mathbf{\Lambda}_s(\mathbf{n}) = \lambda_s \mathbf{n}\otimes\mathbf{n} + \lambda_s^{-1/2}(\mathbf{I} - \mathbf{n}\otimes\mathbf{n})$ is the spontaneous elongation. Minimizing this energy in an infinite planar slab with a clamped foundation is known to generate a standard Biot-type surface instability, with cusped furrows (creases) appearing subcritically at the linear threshold of $\lambda_s \approx 2.27$ [19,27], and being global minimizers beyond the nonlinear nucleation threshold of $\lambda_s \approx 1.77$ [21,27] (SM, Sec. V [25]). We confirm these expectations with 3D finite elements, using a bespoke C code from [22] that divides the slab into constant strain tetrahedra, and moves nodes via damped Newtonian dynamics. These calculations exhibit regular crease lines perpendicular to the director, agreeing with previous elastomer experiments [28] and numerics [22], but disagreeing with the smooth crosshatch in LCEs.

The key additional consideration is that $\mathbf{n}$ can rotate within the LCE, enriching the energy with soft modes. Explicitly minimizing over (unit) directors leads to an energy depending solely on deformation [16],

$$W_I(\mathbf{\Lambda}) = \frac{1}{2}\mu(\Lambda_1^2\lambda_s + \Lambda_2^2\lambda_s + \Lambda_3^2/\lambda_s^2), \qquad \mathrm{Det}\mathbf{\Lambda} = 1, \quad (1)$$

where the Λ_i are the ordered principle stretches. This form matches the *ideal* LCE "trace formula" (with $\lambda_s = r^{1/3}$), originally derived from statistical mechanics [1,29], and is minimized by any $\mathbf{\Lambda}_s(\mathbf{n})$, revealing the degenerate set of ground states [Fig. 2(a)]. Furthermore, the energy is susceptible to microstructure [Figs. 2(a) and 2(b)]. For example, if an LCE cools forming $\mathbf{n} = \hat{\mathbf{y}}$ and is then stretched along $\hat{\mathbf{x}}$, then at an imposed stretch of $\lambda_s^{3/2}$, it will again attain a low energy state with $\mathbf{n} = \hat{\mathbf{x}}$. However, intermediate pure stretches are not soft, as the corresponding

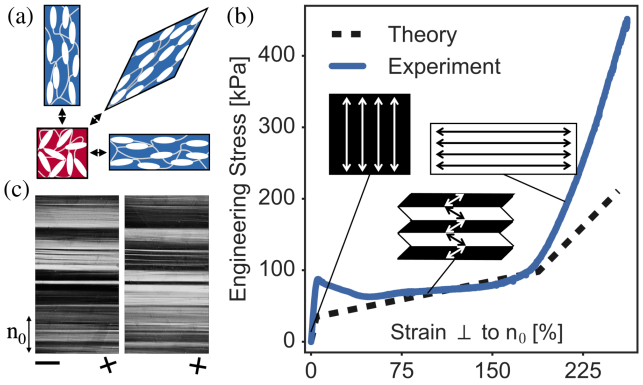

FIG. 2. (a) Soft modes in LCEs. (b) Experimental and theoretical [1] stress-strain curves. Theory parameters: $\lambda_s = 2$, $\alpha = 0.05$, $\mu = 600$ kPa. (c) Micrographs of a stripe microstructure rotated under cross-polarizers. Scale bar 500 μm.

ground states require shear. Nevertheless, the LCE can accommodate pure stretch macroscopically by rapidly switching between bands of alternating shear: a laminar "stripe-domain" microstructure [15] that is geometrically compatible and soft.

More generally, any pure shear can be expressed as $\mathbf{S}(\boldsymbol{\gamma}, \hat{\mathbf{m}}) = \mathbf{I} + \boldsymbol{\gamma}\otimes\hat{\mathbf{m}}$, where $\hat{\mathbf{m}}$ defines the shear plane and $\boldsymbol{\gamma}$, orthogonal, encodes magnitude and direction. A lamination averaging to $\mathbf{\Lambda}$ is then constructed as

$$\mathbf{\Lambda} = f\mathbf{\Lambda}_1 + (1-f)\mathbf{\Lambda}_2, \quad \text{where}$$
$$\mathbf{\Lambda}_1 = \mathbf{S}[(1-f)\mathbf{a}, \hat{\mathbf{m}}]\mathbf{\Lambda} \quad \text{and} \quad \mathbf{\Lambda}_2 = \mathbf{S}(-f\mathbf{a}, \hat{\mathbf{m}})\mathbf{\Lambda}, \qquad (2)$$

and $0 < f < 1$ is the volume fraction of $\mathbf{\Lambda}_1$. If the resultant energy, $fW(\mathbf{\Lambda}_1) + (1-f)W(\mathbf{\Lambda}_2)$, is lower than $W(\mathbf{\Lambda})$, then microstructure is favored. The full relaxation of $W_I(\mathbf{\Lambda})$ has been constructed [16], showing that any $\mathbf{\Lambda}$ with principle stretches less extreme than λ_s may be achieved softly with double laminates. Since this set contains $\mathbf{\Lambda} = \mathbf{I}$, the LCE can microstrucurally accommodate the experimental compression, motivating turbidity but not macroscopic surface instability.

The final missing physics is nonideality: fabrication imprinted a preferred director $\mathbf{n}_0$, breaking degeneracy. Imprinting generates an additional bulk anchoring term (akin to E or B fields in liquid nematics [30]) parametrized by a small coefficient α penalizing rotation away from $\mathbf{n}_0$ [31]:

$$W_{\rm NI}(\mathbf{\Lambda}) = \min_{\mathbf{n}}\Big\{W_{\rm NH}[\mathbf{\Lambda}\mathbf{\Lambda}_s^{-1}(\mathbf{n})] + \frac{1}{2}\alpha\lambda_s\mu \times \mathrm{Tr}[\mathbf{\Lambda}(\mathbf{I} - \mathbf{n}_0\otimes\mathbf{n}_0)\mathbf{\Lambda}^{\rm T}\mathbf{n}\otimes\mathbf{n}]\Big\}. \qquad (3)$$

We again minimize over $\mathbf{n}$ by collecting the relevant terms as $\frac{1}{2}\mu\mathrm{Tr}(\mathbf{M}\mathbf{n}\otimes\mathbf{n})$, and directing $\mathbf{n}$ along $\mathbf{M}$'s minimizing eigenvector. We then implement $W_{\rm NI}$ in finite elements to simulate the LCE slab (SM, Sec. VII [25]). An initial

calculation clamping top and bottom surfaces ($\mathbf{\Lambda} = \mathbf{I}$) produces microstructure suggestive of double lamination but with mesh-scale oscillations in director and deformation (Fig. S11 [25]). Releasing the top produces promising thickness-scale topography, but atop mesh-scale oscillations. Ultimately, this approach is unsatisfactory, as the (nonquasiconvex [16,32]) energy's minimizers are infinitely fine microstructures. Physically, resolution requires a Frank energy $\frac{1}{2}K|\nabla\mathbf{n}|^2$ which smooths director variation over the "nematic penetration depth" $l \sim \sqrt{K/\mu} \sim 10^{-8}$ m [1], regularizing the interfaces [15]. Incorporating Frank energy enables converged mesh-independent results [33], but requires meshes fine compared to l that are infeasible for macroscopic samples.

Instead, we adopt a two-scale approach, first computing the microstructural relaxation of W_{NI} for any average deformation, then using this relaxed energy for macroscopic analysis. This relaxation problem is solved analytically for films in tension [15,17], but a 3D result remains distant so we construct it numerically. The space of 3D deformations $\mathbf{\Lambda}$ is 9D; however, incompressibility, frame indifference, and uniaxial material symmetry allow the energy to be parametrized by just four scalar invariants [34,35]. We may thus reexpress any nematic energy as $W(\mathbf{\Lambda}) = w(\Lambda_1, \Lambda_3, \theta, \phi)$, θ, ϕ being the latitude and longitude of $\mathbf{n}_0$ in the (reference) stretch axes. To relax the energy, we construct a grid of ~50 000 points over this space, spanning $1 \le \Lambda_3 \le 4$ with $\delta\Lambda_3 = 0.1$ resolution, and the remaining three (finite) dimensions with 11 even points each. We then compute a test deformation $\mathbf{\Lambda}_t(\Lambda_1, \Lambda_3, \theta, \phi)$ at each point, matching the invariants, and minimize over "rank-1" laminates:

$$W_{R1}(\mathbf{\Lambda}) = \min_{f,\hat{\mathbf{m}},\mathbf{a}\perp\hat{\mathbf{m}}} fW_{\mathrm{NI}}(\mathbf{\Lambda}_1) + (1-f)W_{\mathrm{NI}}(\mathbf{\Lambda}_2). \quad (4)$$

Minimization over f, $\hat{\mathbf{m}}$, and $\mathbf{a}$ (five d.o.f.) is conducted in *Mathematica*, using simulated annealing and conjugate gradient (SM, Sec. VIII [25]). Interpolation over the grid then yields a numerical approximation of W_{R1} and the lamination parameters. Repeating with W_{R1} produces W_{R2}, while further iterations provide no benefit. For strong convergence, we conduct a final conjugate gradient minimization with analytic derivatives over the full 15 d.o.f. of double lamination. The relaxed first Piola-Kirchhoff stress for the $\mathbf{\Lambda}_t$ at each point is then computed as the volume-weighted sum of the four constituent stresses, themselves evaluated as analytic derivatives $P_{\mathrm{NI}_{ij}} = (\partial W_{\mathrm{NI}}/\partial\Lambda_{ij})$ (SM, Sec. VI [25]). Interpolation yields a numerical stress for any $\mathbf{\Lambda}_t$, which we rotate to produce the stress for any $\mathbf{\Lambda}$.

In Fig. 3 we show two resulting energy and force-extension curves: uniaxial stretch along $\mathbf{n}_0$ and simple shear perpendicularly. In both, microstructure occurs over a finite region, convexifies the energy, and eliminates discontinuities and negative stress gradients. Uniaxial stretching experiments

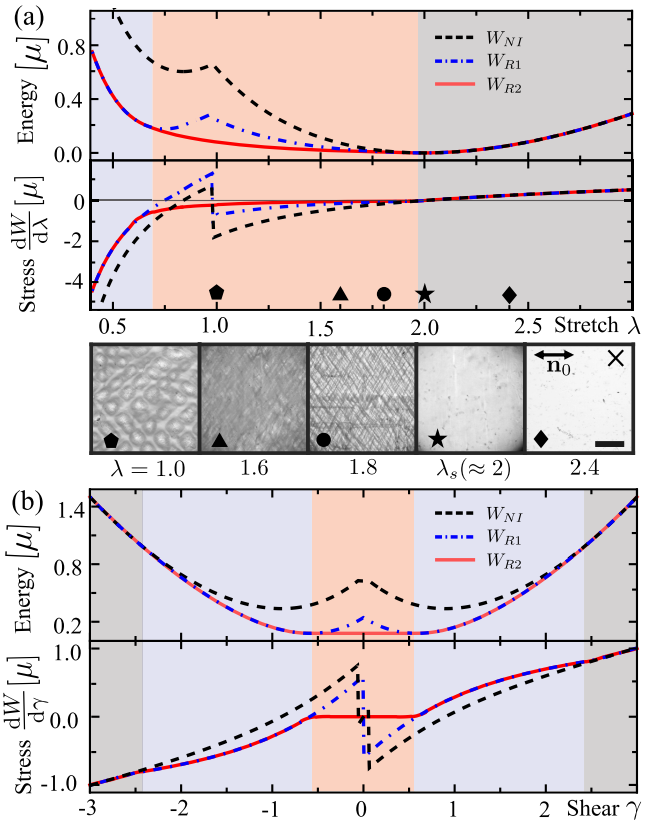

FIG. 3. Energy and stress upon (a) uniaxial stretch $\mathbf{\Lambda} = \lambda\mathbf{n}_0 \otimes \mathbf{n}_0 + \lambda^{-1/2}(\mathbf{I} - \mathbf{n}_0 \otimes \mathbf{n}_0)$ and (b) simple shear $\mathbf{\Lambda} = \mathbf{I} + \gamma(\mathbf{n}_0 \times \mathbf{n}_0^{\perp}) \otimes \mathbf{n}_0^{\perp}$. Gray domain, no microstructure; blue, first-order laminate; red, second-order laminate. (a) bottom: POM of experimental samples ($t = 170$ μm; scale bar 500 μm) showing microstructure evolution under uniaxial strain. $\lambda = 1$ shows surface instability, $1 < \lambda < \lambda_s$ shows crosshatch microstructure, and $\lambda \ge \lambda_s$ is a clear monodomain.

(by adhering at intermediate temperatures) show a very fine microstructure generating a hazy appearance in the expected region, which coarsens into a visible crosshatch microstructure and then ultimately vanishes as the relaxed monodomain state λ_s is approached [Fig. 3(a)]. Samples adhered at $\lambda = 1$ also show the macroscopic surface instability, but these large features contain the fine microstructural crosshatches within (see Movie M4 and Fig. S8 [25]) justifying our two-scale approach. An additional test case, perpendicular stretching of a sheet (Fig. S13 [25]), agrees with analytic results [15,17]. Corresponding experiments [Fig. 2(b)] confirm a stress plateau (and lamination) consistent with material values $\alpha \approx 0.05$, $\lambda_s \approx 2$.

Having tested the relaxed energy and stress functions, we minimize to predict the surface instability. We consider an LCE slab initially occupying $-t < z < 0$, that is clamped below, free above, and has planar $\mathbf{n}_0 = \hat{\mathbf{x}}$. The final configuration minimizes the total energy $W = \int W_N(\mathbf{\Lambda})\mathrm{d}V$ over permitted displacement fields $\mathbf{u}$, requiring stress balance, $\partial_i P_{ij} = 0$, with $\mathbf{P} \cdot \hat{\mathbf{z}} = 0$ on top. We first

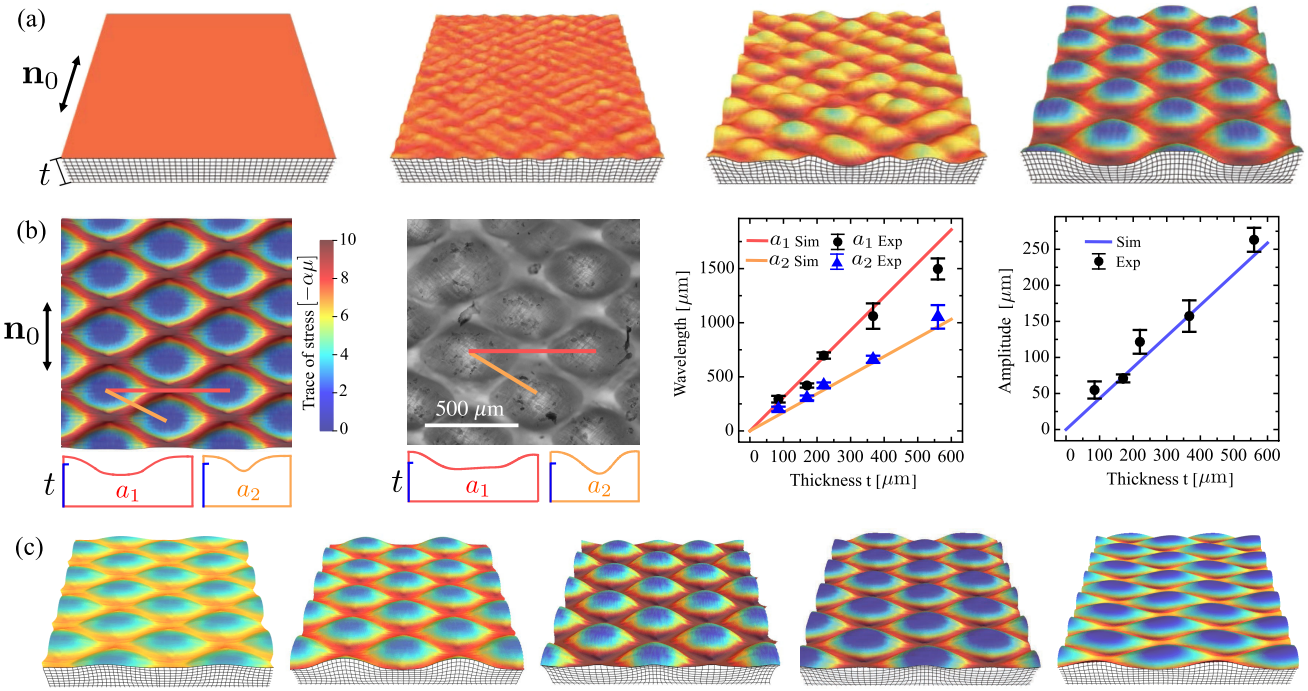

FIG. 4. (a) Dynamics and coarsening of the surface instability with $(\lambda_s, \alpha) = (2, 0.05)$. (b) Comparison of experimental ($t = 220$ μm) and numerical $(\lambda_s, \alpha) = (2, 0.05)$ topography. Wavelengths measured in POM, line profiles and amplitude from optical and scanning profilometry, errors are one standard deviation, $n = 10$. (c) Simulated topography for $(\lambda_s, \alpha) = (1.44, 0.05), (1.71, 0.05), (2.15, 0.05), (2.15, 0.15), (2.15, 0.3)$.

minimize using finite elements (SM, Secs. IV and X [25]). For simplicity, we mimic incompressibility by taking W_N as compressible but with a large bulk modulus of $B = 100\mu$:

$$W_N(\mathbf{\Lambda}) = W_{R2}(\mathbf{\Lambda}/\mathrm{Det}\mathbf{\Lambda}^{1/3}) + \frac{1}{2}B(\mathrm{Det}\mathbf{\Lambda} - 1)^2. \quad (5)$$

An initial computation considers a near square slab $(6.24t \times 6t)$ divided into 126 000 elements of size $0.06t$. The LCE is modeled with $\lambda_s = 2$, $\alpha = 0.05$, and initialized at $\mathbf{\Lambda} = \mathbf{I}$. As seen in Fig. 4(a) and SM Movie M5 [25], the free surface immediately destabilizes to oblique mesh-scale ripples, which coarsen via dynamics into an equilibrium crosshatch strongly resembling experiment. We then use fine-mesh calculations on geometrically optimized unit cells to find the exact minimizers for a range of λ_s and α (i.e., different LCEs). All are unstable, but with lower amplitude at lower λ_s, and shifting wave vectors at higher α [Fig. 4(c)]. The range of α explored spans the reported range for physical monodomain LCEs [15], suggesting the crosshatch instability is ubiquitous in LCEs under compression. Equilibrium amplitude and wavelength are necessarily simply proportional to the problem's only length scale t, and in good agreement with experiment. Moreover, unlike creasing, all topography is smooth and noncontacting.

Linear stability analysis offers further insight. Owing to finite compressibility, the equilibrium equations admit a transitionally invariant base state $\mathbf{\Lambda}_0 = \mathbf{I} + \gamma\hat{\mathbf{z}} \otimes \hat{\mathbf{z}}$, where $\gamma \sim \alpha\mu/B \sim 10^{-5}$. Following Biot [19], we consider an infinite depth slab (half-space), and add a small incremental displacement, $\mathbf{u} = \gamma\hat{\mathbf{z}} + \epsilon\mathbf{u}_1$, giving $\mathbf{\Lambda} = \mathbf{\Lambda}^0 + \epsilon\mathbf{\Lambda}^1$. Since perturbations are about equilibrium, energy varies quadratically:

$$W_N = W_N(\mathbf{\Lambda}^0) + \frac{1}{2}\epsilon^2 \left.\frac{\partial^2 W_N}{\partial\Lambda_{ij}\partial\Lambda_{lm}}\right|_{\mathbf{\Lambda}^0} \Lambda^1_{ij}\Lambda^1_{lm}. \quad (6)$$

Minimizing variationally over displacement gives the incremental equilibrium equations, $\partial_i P^1_{ij} = 0$ and $\mathbf{P}^1\hat{\mathbf{z}} = 0$, where $P^1_{ij} = (\partial^2 W_N/\partial\Lambda_{ij}\partial\Lambda_{lm})|_{\mathbf{\Lambda}_0}\Lambda^1_{lm}$. Many of these derivatives are zero via uniaxial material symmetry. The remainder, we compute using finite differences, reducing the energy to a quadratic in $\nabla\mathbf{u}_1$, and the stress equations to linear constant-coefficient ordinary differential equations. To compute accurate derivatives, we explicitly reminimize W_{R2} at the finite-difference points, revealing additional zero curvatures corresponding to vanishing incremental moduli for shearing perpendicular to $\mathbf{n}_0$ [cf. the W_{R2} plateau in Fig. 3(b)]. Such vanishing moduli have been observed at the onset of monodomain striping [30,36] but are here deep within the microstructure region. The underlying cause is that optimal lamination involves four equivalent deformations, and such shears are accommodated by rearranging volume fractions, similar to how, in 1D, curvature vanishes after common-tangent convexification.

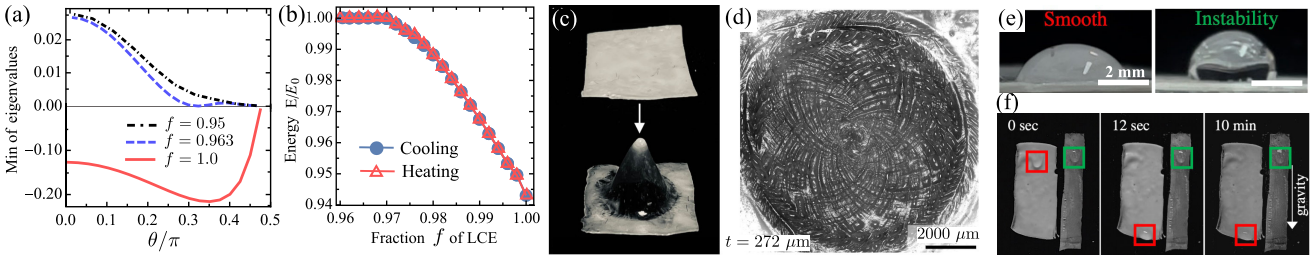

FIG. 5. (a),(b) Analysis of onset. (a) Minimal Hessian eigenvalue vs angle for $f = 0.95$ (stable), $f = f_c = 0.963$ (instability threshold), and $f = 1.0$ (pure LCE, unstable). For $f = 1$, the minimum eigenvalue has $\theta_c \approx 0.35\pi$. (b) Cooling and heating FEM showing supercritical onset at $f_c \approx 0.97$. E_0 is the base-state energy. (c)–(f) Experimental extensions. (c) Mechanically programmed LCE cone. (d) Micrograph of resulting log-spiral surface instability. (e) Photographs of a 15 μl water droplet on room temperature LCEs ($t = 170$ μm) with smooth and unstable surfaces: instability changes the contact angle. (f) Similar droplet running down vertical surfaces: instability promotes pinning.

To solve, we substitute an ansatz that decays with depth, $\mathbf{u}_1 = \exp(k\lambda z)\mathbf{v}(x, y)$, and undulates in plane with k vector along $\mathbf{x}'$, forming an angle θ with $\mathbf{x}$:

$$\mathbf{v} = c_h \cos(kx')\hat{\mathbf{x}}' + c_g \cos(kx')\hat{\mathbf{y}}' + \sin(kx')\hat{\mathbf{z}}.$$

Substituting into the stress equations (SM, Sec. XI [25]) trigonometric, exponential, and k factors all cancel, leaving dimensionless algebraic equations for c_g, c_h, and λ. Solving for $c_g(\lambda)$ and $c_h(\lambda)$ reveals a final quadratic in λ^2 giving two decaying roots (λ_1, λ_2), and hence,

$$\mathbf{u}_1 = c_1 \exp(k\lambda_1 z)\mathbf{v}(\lambda_1) + c_2 \exp(k\lambda_2 z)\mathbf{v}(\lambda_2).$$

We then substitute $\mathbf{u}_1$ into the energy and integrate, yielding a quadratic in c_1, c_2. Stability follows from the Hessian, with negative eigenvalues indicating growing perturbations. Inevitably given the scale-free character, stability is independent of k. More surprisingly, despite uniaxial symmetry, all angles are unstable. We thus assess relative growth rates from the eigenvalue's magnitude, revealing an oblique perturbation grows fastest [Fig. 5(a)], motivating the crosshatch.

To study onset, we imitate a cooling LCE via the energy $(1 - f)W_{\mathrm{NH}}(\mathbf{\Lambda}) + fW_{R2}(\mathbf{\Lambda})$, with f a temperature proxy. Both finite-elements and linear analysis show onset around $f \approx 0.96$. Furthermore, finite elements show onset is supercritical, with topography appearing continuously and without hysteresis [Fig. 5(b)], unlike the strong subcriticality of Biot creasing.

Our work thus shows that the exotic constitutive law of LCEs still supports a compressive surface instability, with similar scale-free properties to Biot creasing, but also fundamental differences in pattern, criticality, and singularity. We anticipate similar behavior will be found in other soft solids with distinctive constitutive laws: highly anisotropic solids (fiber reinforced elastomers, biological tissues), phase-changing solids, active nematic solids, and mechanistic metamaterials are all important and analogous examples. Hopefully, such studies will also generate a stronger intuition for Biot-type instabilities, and ultimately enable a predictive analytic framework. Within LCEs, our rigorously homogenized constitutive law also enables quantitative mechanical engineering including studies of other instabilities [37–42], and our homogenization approach will similarly enable analysis of other phase-changing materials [13,43,44].

The LCE surface instability is also an exemplar of instabilities providing complex morphing without correspondingly complex fabrication. A limitation is that this approach provides little control over pattern. However, some more complex morphing may be regained by combining instability with simple patterned fabrication. As an example, we repeat our experiment, using an LCE slab containing a radial director pattern (fabricated by forming a cone during programming), which generates crosshatches in a striking log spiral [Figs. 5(c) and 5(d)]. The instability's switchable high amplitude topography suggests applications in smart surfaces. For example, a droplet sitting atop the instability [Figs. 5(e) and 5(f)] forms a Wenzel state [45,46] with both a higher contact angle and stronger pinning than one atop an identical smooth LCE. Such hydrophobic pinning is observed on rose petals, which have a strikingly similar topography [47,48]. Further smart-surface applications could include switchable aerodynamics, haptics, adhesion, and friction.

This work was supported by a UKRI "future leaders fellowship" grant (Grant No. MR/S017186/1).

*These authors contributed equally to this work.
†jsb56@cam.ac.uk

[1] M. Warner and E. M. Terentjev, *Liquid Crystal Elastomers* (Oxford University Press, New York, 2007), Vol. 120.
[2] J. Küpfer and H. Finkelmann, Nematic liquid single crystal elastomers, Makromol. Chem. **12**, 717(R) (1991).
[3] P.-G. De Gennes, M. Hébert, and R. Kant, Artificial muscles based on nematic gels, Macromol. Symp. **113**, 39 (1997).

[4] T. J. White and D. J. Broer, Programmable and adaptive mechanics with liquid crystal polymer networks and elastomers, Nat. Mater. **14**, 1087 (2015).
[5] C. Modes, K. Bhattacharya, and M. Warner, Gaussian curvature from flat elastica sheets, Proc. R. Soc. A **467**, 1121 (2011).
[6] T. Guin, M. J. Settle, B. A. Kowalski, A. D. Auguste, R. V. Beblo, G. W. Reich, and T. J. White, Layered liquid crystal elastomer actuators, Nat. Commun. **9**, 2531 (2018).
[7] H. Aharoni, Y. Xia, X. Zhang, R. D. Kamien, and S. Yang, Universal inverse design of surfaces with thin nematic elastomer sheets, Proc. Natl. Acad. Sci. U.S.A. **115**, 7206 (2018).
[8] M. Barnes and R. Verduzco, Direct shape programming of liquid crystal elastomers, Soft Matter **15**, 870 (2019).
[9] L. Golubović and T. C. Lubensky, Nonlinear elasticity of amorphous solids, Phys. Rev. Lett. **63**, 1082 (1989).
[10] M. Warner, P. Bladon, and E. Terentjev, Soft elasticity—Deformation without resistance in liquid crystal elastomers, J. Phys. II **4**, 93 (1994).
[11] K. Urayama, S. Honda, and T. Takigawa, Deformation coupled to director rotation in swollen nematic elastomers under electric fields, Macromolecules **39**, 1943 (2006).
[12] D. Corbett and M. Warner, Deformation and rotations of free nematic elastomers in response to electric fields, Soft Matter **5**, 1433 (2009).
[13] K. Bhattacharya, *Microstructure of Martensite: Why it Forms and How it Gives Rise to the Shape-Memory Effect*, Oxford Series on Materials Modelling Vol. 2 (Oxford University Press, New York, 2003).
[14] G. Verwey, M. Warner, and E. Terentjev, Elastic instability and stripe domains in liquid crystalline elastomers, J. Phys. II **6**, 1273 (1996).
[15] H. Finkelmann, I. Kundler, E. Terentjev, and M. Warner, Critical stripe-domain instability of nematic elastomers, J. Phys. II **7**, 1059 (1997).
[16] A. DeSimone and G. Dolzmann, Macroscopic response of nematic elastomers via relaxation of a class of SO(3) invariant energies, Arch. Ration. Mech. Anal. **161**, 181 (2002).
[17] S. Conti, A. DeSimone, and G. Dolzmann, Semisoft elasticity and director reorientation in stretched sheets of nematic elastomers, Phys. Rev. E **66**, 061710 (2002).
[18] J. Biggins, Textured deformations in liquid crystal elastomers, Liq. Cryst. **36**, 1139 (2009).
[19] M. A. Biot, Mechanics of Incremental Deformations (Wiley, New York, 1965).
[20] V. Trujillo, J. Kim, and R. C. Hayward, Creasing instability of surface-attached hydrogels, Soft Matter **4**, 564 (2008).
[21] E. Hohlfeld and L. Mahadevan, Unfolding the sulcus, Phys. Rev. Lett. **106**, 105702 (2011).
[22] T. Tallinen, J. S. Biggins, and L. Mahadevan, Surface sulci in squeezed soft solids, Phys. Rev. Lett. **110**, 024302 (2013).
[23] A. E. Shyer, T. Tallinen, N. L. Nerurkar, Z. Wei, E. S. Gil, D. L. Kaplan, C. J. Tabin, and L. Mahadevan, Villification: How the gut gets its villi, Science **342**, 212 (2013).
[24] T. Tallinen, J. Y. Chung, J. S. Biggins, and L. Mahadevan, Gyrification from constrained cortical expansion, Proc. Natl. Acad. Sci. U.S.A. **111**, 12667 (2014).
[25] See Supplemental Material at http://link.aps.org/supplemental/10.1103/PhysRevLett.131.238101 for the supporting movies, experimental details, numerical methods, and theoretical analysis.
[26] C. Yakacki, M. Saed, D. Nair, T. Gong, S. Reed, and C. Bowman, Tailorable and programmable liquid-crystalline elastomers using a two-stage thiol–acrylate reaction, RSC Adv. **5**, 18997 (2015).
[27] W. Hong, X. Zhao, and Z. Suo, Formation of creases on the surfaces of elastomers and gels, Appl. Phys. Lett. **95**, 111901 (2009).
[28] S. Cai, D. Chen, Z. Suo, and R. C. Hayward, Creasing instability of elastomer films, Soft Matter **8**, 1301 (2012).
[29] P. Bladon, E. M. Terentjev, and M. Warner, Transitions and instabilities in liquid crystal elastomers, Phys. Rev. E **47**, R3838 (1993).
[30] F. Ye, R. Mukhopadhyay, O. Stenull, and T. C. Lubensky, Semisoft nematic elastomers and nematics in crossed electric and magnetic fields, Phys. Rev. Lett. **98**, 147801 (2007).
[31] G. Verwey and M. Warner, Compositional fluctuations and semisoftness in nematic elastomers, Macromolecules **30**, 4189 (1997).
[32] J. M. Ball, Convexity conditions and existence theorems in nonlinear elasticity, Arch. Ration. Mech. Anal. **63**, 337 (1976).
[33] H. Zhou and K. Bhattacharya, Accelerated computational micromechanics and its application to polydomain liquid crystal elastomers, J. Mech. Phys. Solids **153**, 104470 (2021).
[34] A. J. M. Spencer, *Deformations of Fibre-Reinforced Materials* (Clarendon Press, Oxford, 1972).
[35] M. Destrade, B. M. Donald, J. Murphy, and G. Saccomandi, At least three invariants are necessary to model the mechanical response of incompressible, transversely isotropic materials, Comput. Mech. **52**, 959 (2013).
[36] J. S. Biggins, E. M. Terentjev, and M. Warner, Semisoft elastic response of nematic elastomers to complex deformations, Phys. Rev. E **78**, 041704 (2008).
[37] L. A. Mihai and A. Goriely, Instabilities in liquid crystal elastomers, MRS Bull. **46**, 784 (2021).
[38] A. Giudici and J. S. Biggins, Giant deformations and soft-inflation in LCE balloons, Europhys. Lett. **132**, 36001 (2020).
[39] V. Lee and K. Bhattacharya, Actuation of cylindrical nematic elastomer balloons, J. Appl. Phys. **129**, 114701 (2021).
[40] V. Lee and K. Bhattacharya, Universal deformations of incompressible nonlinear elasticity as applied to ideal liquid crystal elastomers, J. Elast. (2023).
[41] M. S. Krieger and M. A. Dias, Tunable wrinkling of thin nematic liquid crystal elastomer sheets, Phys. Rev. E **100**, 022701 (2019).
[42] A. Goriely and L. A. Mihai, Liquid crystal elastomers wrinkling, Nonlinearity **34**, 5599 (2021).
[43] J. Adams, S. Conti, and A. DeSimone, Soft elasticity and microstructure in smectic C elastomers, Continuum Mech. Thermodyn. **18**, 319 (2007).
[44] H. Gu, J. Rohmer, J. Jetter, A. Lotnyk, L. Kienle, E. Quandt, and R. D. James, Exploding and weeping ceramics, Nature (London) **599**, 416 (2021).

[45] R. N. Wenzel, Resistance of solid surfaces to wetting by water, Ind. Eng. Chem. **28**, 988 (1936).
[46] A. Lafuma and D. Quéré, Superhydrophobic states, Nat. Mater. **2**, 457 (2003).
[47] D. Roy, K. Pandey, M. Banik, R. Mukherjee, and S. Basu, Dynamics of droplet impingement on bioinspired surface: Insights into spreading, anomalous stickiness and break-up, Proc. R. Soc. A **475**, 20190260 (2019).
[48] S. V. Oopath, A. Baji, and M. Abtahi, Biomimetic rose petal structures obtained using UV-nanoimprint lithography, Polymers (Basel) **14**, 3303 (2022).